J Mater Sci (2023) 58:302–316

Electronic materials

Preparation of C–TiO_2 photocatalyst with Ti_3C_2 MXene as precursor by molten salt method and its hydrogen production performance

Xinxin Jin[1], Minmin Yan[1], Yanli Zhuang[1], Limin Dong[1,*], Haixia Wang[1], Hao Niu[1], Shaokai Hou[1], Lianwei Shan[1], Xiao Li[1], and Fengming Zhang[1,*]

[1] *School of Materials Science and Chemical Engineering, Harbin University of Science and Technology, Harbin 150040, People's Republic of China*

Received: 12 June 2022
Accepted: 18 November 2022
Published online:
1 January 2023

ABSTRACT

In this paper, Ti_3C_2 was completely oxidized at a high temperature (350 °C, 400 °C and 450 °C) to form a composite catalysts: TiO_2 nanoparticles with fragmentary carbon supporting, using the $ZnCl_2$ molten salt method. The generated disordered carbon forms an inseparable connection with TiO_2 nanoparticles grown in situ on the surface, which reduces the recombination of photocarriers and increases the specific surface area. $ZnCl_2$ plays an important role in delaying the oxidation rate, thus inhibiting the abnormal growth of TiO_2 grain and retaining more carbon, which led to a suitable composition of the catalyst, so as to obtain a better hydrogen production performance. $ZnCl_2$ existence might also prevent the collapse of the accordion structure during the calcination process. The hydrogen production activity of C–TiO_2 photocatalyst prepared by molten salt method with 3 wt% Pt as cocatalyst is up to 2.3 mmol/g/h, about 5.4 times and 2 times of that of calcination without molten salt and pure P25, respectively.

Handling Editor: Kyle Brinkman.

Address correspondence to E-mail: donglm@hrbust.edu.cn; zhangfm80@163.com

https://doi.org/10.1007/s10853-022-07991-2

GRAPHICAL ABSTRACT

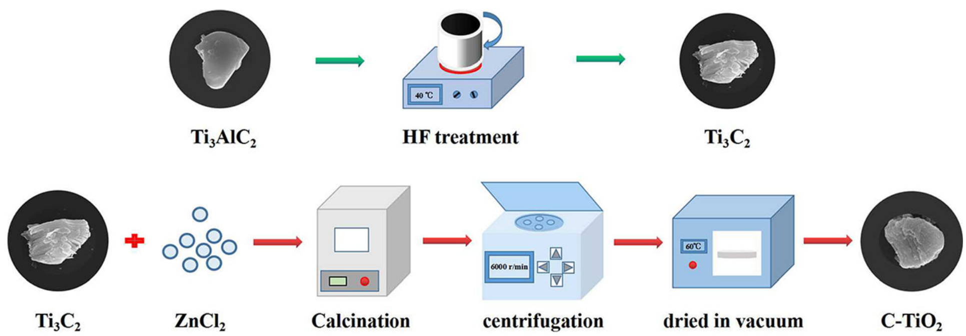

Introduction

Environmental pollution and energy crisis are the two major issues that urgently need to be solved [1]. Hydrogen (H_2), as a kind of renewable green energy, with high combustion value and free pollution, has been widely concerned by researchers. The principle of photocatalysis is to convert the inexhaustible solar energy into chemical energy by using semiconductor photocatalysts [2, 3], which is considered to be one of the most effective strategies to prepare hydrogen energy [4, 5]. Hydrogen production performance of catalysts mainly depends on their absorption capacity of sunlight, the separation and transference efficiency of the generated photocarriers and the quantity of active sites on the reaction surface [6–8].

TiO_2 has been widely used in the fields of H_2 generation and pollutant degradation due to the advantages of cost-effective and simple preparation process and plays an important role in various photocatalytic and photo-electrocatalytic processes because of the suitable H^+ reduction potential, environmental friendliness and excellent chemical stability [9]. However, the photocatalytic performance of TiO_2 is seriously limited owing to the large band-gap energy (3.2 eV), causing the mere absorption of UV light and rapid recombination of photocarriers, which greatly hinders its utilization of sunlight and H_2 production efficiency [10, 11]. Currently, the modification of TiO_2 is addressed to solve the issues above, and the common methods adopted include the element doping, heterojunction construction, precious metal deposition and crystal plane regulation [12–14]

In recent years, the interest in two-dimensional (2D) photocatalysts has been increasing. MXenes is a general term for 2D transition metal carbides and carbonitrides with remarkable electronic conductivity [15–17]. Ti_3C_2, as one of the most widely studied members of MXenes since 2011, has been synthesized by etching aluminum atoms in layered Ti_3AlC_2. The unique accordion-like structure of Ti_3C_2 has a high specific surface area, which can provide a large number of active sites for photocatalysts materials to exhibit high photocatalytic H_2 evolution [18, 19]. The surface of Ti_3C_2 usually contains hydrophilic groups, such as –O, –OH [20, 21], which is favorable for the H_2 products. Due to the distinct advantages, it is effective for Ti_3C_2 to compound with most semiconductor materials [22–30]. When Ti_3C_2 was strongly oxidized, TiO_2 generated. As further oxidation proceeded, the Ti_3C_2 disappeared, some carbon oxidized to produce CO_2 and the left C-layers were covered with TiO_2. Therefore, C–TiO_2 was produced [31, 32]. C can promote the separation of electrons and holes and narrow the band gap. Therefore, C–TiO_2 is considered to be a potential photocatalyst [12, 14]. At present, Naguib et al. [33]. proved that Ti_3C_2 powder could be rapidly oxidized by calcination at 1150 °C for 30 s, and that TiO_2 nanocrystals were obtained to grow inter-layers and at the edge of layers, and embedded into the disordered graphite carbon structure. The studies proved that the in situ growth of TiO_2 on the surface of multilayer Ti_3C_2 was achieved by calcination and hydrothermal treatment [34]. These studies indicated the feasibility of in situ growth of TiO_2 on Ti_3C_2 nanosheets. At present, Shu Wang et al. [35] used tetrabutyl titanate (TBOT) as raw materials to prepare C/TiO_2 by sol–gel method with a H_2 evolution rate of 0.577 mmol/h/g, which reached 1.560 mmol/h/g after reduction treatment. Yang et al. [36] showed that TiC@C–TiO_2 cored-shell photocatalyst was prepared by calcination of TiC, and the maximum H_2 production capacity was 0.558 mmol/g. Guangri et al. [31] synthesized C–TiO_2 under low-temperature hydrothermal treatment of Ti_3C_2. The H_2 yield reaches 0.033 mmol/h/g. Yuan et al. [32] obtained the C/TiO_2 composites by oxidizing Ti_3C_2 in a CO_2 atmosphere, and the optimal H_2 evolution rate under visible light could reach 0.024 mmol/h/g. Based on the above work, the highest yield of hydrogen for TiO_2/C currently investigated is 1.560 mmol/h/g.

Molten salt method is to take one or more salts with low melting point in the molten state as the calcination medium and the raw material is placed in the molten salt system for reaction. Crystal growth is in the liquid molten salt under which the morphology is easily controlled [37]. Molten salt method has the advantages of better crystal morphology, simple operation, and lower synthesis temperature compared with those without salts.

In this paper, C–TiO_2 was prepared with molten salt method. Ti_3C_2 was used as the precursor, and $ZnCl_2$ was added as the molten salt. C–TiO_2 catalyst was prepared at different temperatures (350, 400 and 450 °C) by molten salt method. The effect of the addition of $ZnCl_2$ during the process of calcination on C–TiO_2 growth was investigated for the photocatalytic hydrogen production performance. In this design, the "accordion" structure of C–TiO_2 was tested by photoluminescence spectra to discuss the diffusion recombination for photoexcited electrons and holes, by UV–visible diffuse reflectance to discuss UV–visible light utilization capacity, and by electrochemical test to study the separation and transfer efficiency of photocarriers.

Materials and methods

Materials

All chemical reagents were analytical grade and used directly without further purification: HF (49%, Shanghai McLin Biochemical Technology Co., Ltd), Ti_3AlC_2 (> 98% purity, Shanghai McLin Biochemical Technology Co., Ltd.), triethanolamine (Tianjin Fuyu Fine Chemical Co., Ltd.), $H_2PtCl_6·6H_2O$ (Tianjin Guangfu Fine Chemical Research Institute), and the deionized water (Harbin Yongchang Chemical Reagent Company).

Methods

Synthesis of Ti_3C_2 MXenes

2 g of Ti_3AlC_2 was powdered into a plastic beaker, and 50 mL 49% HF solution slowly was add for etching. After ultrasonic for 8 h (KQ-600DE, Kunshan Ultrasound Instrument Co., Ltd), the solution was placed into a water bath and stirred at 40 °C for 72 h. Then the suspension was washed with deionized water and centrifuged (H1850, Xiangyi Centrifuge Instrument Co., Ltd) for dozens of times until pH > 6. Finally, the solution was poured into petri dishes and dried in vacuum at 60 °C for 12 h. The black powder Ti_3C_2 was obtained, then which was grinded with an agate mortar and stored in a brown bottle away from light.

Synthesis of C–TiO_2 composites

Briefly, 0.2 g of Ti_3C_2 and 1 g of $ZnCl_2$ were placed into a quartz crucible and mix them evenly and calcined at 350 °C, 400 °C and 450 °C for 4 h in muffler furnace (KSL-1100X, Shuyan Heat Treatment Equipment Manufacturing Co., LTD.). Heating rate was 5 °C/min. The samples were thoroughly washed with dilute hydrochloric acid solution and washed and centrifuged 6 times with deionized water and anhydrous ethanol at 5000 rad/min. After vacuum drying at 60 °C for 12 h, the gray powder C–TiO_2 was obtained. Finally, grind it with an agate mortar and store in a brown bottle away from light. 0.2 g Ti_3C_2 was calcined at 400 °C for 4 h as control group. The samples were named T-Z-350, T-Z-400, T-Z-450 and T-400, respectively. Moreover, 0.6 g and 1.4 g of $ZnCl_2$ molten salts were used for 0.2 g of Ti_3C_2 calcination under 400 °C for comparison and the calcined sample was named for T-Z_l-400 and T-Z_m-400, respectively.

Characterization

Room temperature X-ray diffraction measurements were characterized by powder X-ray diffractometer (XRD, Netherlands, X'Pert PRO) in the range of 40 kV, 40 mA, 2θ 5–80°. The microscopic morphology images of samples were obtained using transmission electron microscope (TEM, Japan, JEM-2100) and scanning electron microscope (SEM, Netherlands, FEI Sirion 200). The elemental compositions of catalysts were determined using X-ray fluorescence (XRF, PANalytical Axios). The elementary composition and valence state of samples were tested by the X-ray photoelectron spectroscopy (XPS, USA, ESCALAB 250Xi). The crystal structure of the material is determined using a Raman spectrometer (Raman, USA, DXR Microscope). Fourier transform infrared spectra were tested by a Fourier transform infrared spectrometer (FT-IR, USA, NICOLET iS10). Photoluminescence spectra were evaluated on a fluorescence spectrophotometer (pL, Japan, RF-5301PC). The UV–visible diffuse reflectance spectra of the samples were recorded on a UV–visible spectrophotometer (DRS, Japan, UV-2600i) with barium sulfate fine powder as control. The Bruner–Emmett–Taylor specific area (S_{BET}) of the sample was measured by N_2 adsorption at liquid nitrogen temperature (BET, USA, ASAP 2010). The photochemical properties of the samples were tested by a electrochemical workstation (China, CHI660E) using a three-electrode system. 2 mg of the sample was added to a mixture of 1 mL ethanol and 10 μL naphthol, and the suspension (200 μL) was dropped onto the ITO glass substrate and dried at room temperature. Electrochemical impedance spectroscopy (EIS) was carried out using ITO coated with photocatalyst as working electrode, platinum as counter electrode, saturated calomel as reference electrode, and Na_2SO_4 solution (0.25 M) as electrolyte. Mott-Schottky tested at frequencies of 500 Hz, 700 Hz, and 900 Hz, with potentials ranging from − 0.4 V to 0.4 V and an AC voltage amplitude of 5 mV. The combination of visible light filter ($\geq$ 420 nm) and 300 W Xe lamp was used as the light source to test the photocurrent-time curve.

Photocatalytic hydrogen production

The photocatalytic hydrogen production experiment was tested in the all-glass Automatic online Trace Gas Analysis System (China, Labsolar-6A). The photocatalytic experiment was tested as follows. First, 10 mg of the photocatalyst was added to 50 mL triethanolamine (TEOA) aqueous solution (20 wt%). Then, 3 wt% chloroplatinic acid solution was used as the cocatalyst, and the mixed solution was placed in an ultrasound machine for 30 min. Under the irradiation of 300 w Xe lamp, chloroplatinic acid solution was used as the precursor, and Pt was in situ supported on the photocatalyst by photo-deposition. During the whole photocatalytic reaction, water cooling at 5 °C was maintained, and the reaction solution was continuously stirred to keep the mixture evenly distributed. Vacuum the system with a vacuum pump to make the system pressure close to 0.8 kPa, so as to ensure the vacuum state of the internal system. The generated H_2 was detected by gas chromatograph (China, Techcomp GC9790) and thermal conductivity detector (TCD) every 60 min.

Results and discussion

XRD and XRF analysis

XRD test was used to investigate the crystal structure. The typical diffraction peaks of Ti_3AlC_2 (JCPDS No. 52-0975) at 9.5°, 19.1°, 34.0°, 38.7°, 41.7° and 56.4° are shown in Fig. 1a (bottom). After HF etching, the diffraction peaks at the 2θ of 8.8°, 18.3°, 27.5°, 36.9° and 41.9° appeared as shown in Fig. 1a (top). In addition, the diffraction peak at 2θ = 38.7° disappeared with HF etching, indicating that the aluminum atom layer was completely removed and Ti_3C_2 samples have been successfully prepared [38]. Figure 1b shows the XRD patterns of the samples obtained under different preparation conditions. The sharped peaks at the 2θ of 25.1°, 37.7°, 47.9°, 53.9° and 62.5° are related to the plane diffraction of (101), (004), (200), (105) and (204) of anatase TiO_2 (JCPDS No. 21-1272), respectively. It indicates that Ti_3C_2 has been transformed into anatase TiO_2 by calcination. By comparing the XRD curves of T-Z-350, T-Z-400, T-Z-450 and T-400, it can be seen that with the increase of calcination temperature, the diffraction peak corresponding to TiO_2 gradually enhanced, indicating that the crystallinity of TiO_2 is improved. The particle size of TiO_2 can be calculated by Scherrer formula [39], expressed as $D = K\lambda/(\beta\cos\theta)$ (K stands for constant; λ stands for the wavelength of X-ray; β is half width of diffraction peak; θ is diffraction angle). The grain

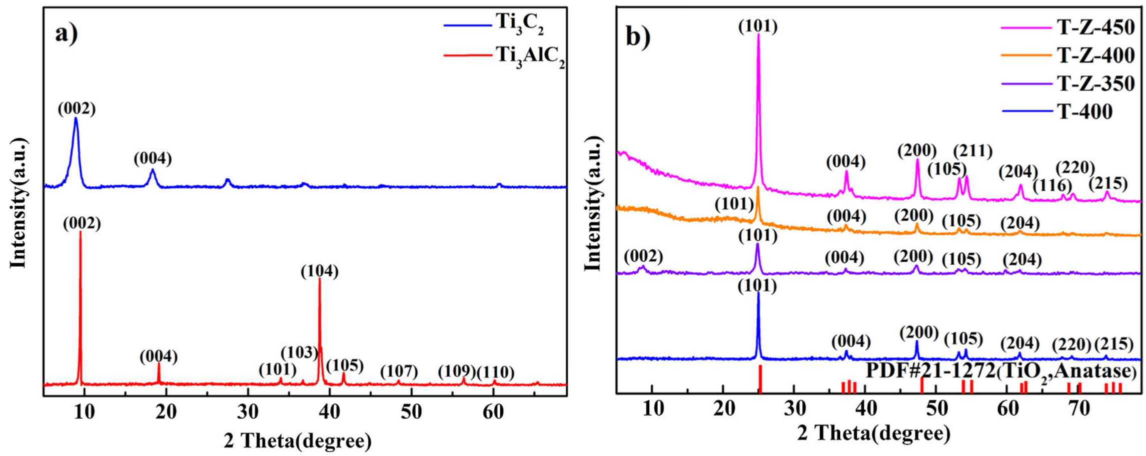

Figure 1 The XRD pattern of **a** Ti_3C_2; **b** T-400, T-Z-350, T-Z-400 and T-Z-450..

sizes of T-Z-400 and T-400 are 23.19 nm and 30.84 nm. Comparing T-Z-400 and T-400 prepared at the same temperature, it can be seen that the TiO_2 prepared by molten salt method has smaller grain size.

In addition, XRD can also reflect the relative yield of TiO_2 to a certain extent. The characteristic peak value of T-400 is the highest, followed by T-Z-450, and the lower peak value is for the T-Z calcinated at lower temperature. XRF results (Table 1) shows the mass fraction content of TiO_2 in each catalyst. At the same calcination temperature (400 °C), the existence of molten salts resisted the direct contact between external gas and Ti_3C_2 and therefore reduced the oxidation rate of Ti_3C_2 compared with that by the direct calcination without molten salts resulting in the highest TiO_2 content: 93.71 wt%. However, in the presence of molten salt, the higher the calcination temperature was, the more TiO_2 was produced and the better the crystallinity was, which is easy to understand: high temperature provides high energy, accelerates the flow of oxygen, and accelerates the oxidation rate of the sample; thus, more TiO_2 is generated. XRF cannot determine the content of element C, and the content of C is not given here. Moreover, T-Z-350 contains less TiO_2 determined by XRF, which also indicates that part of Ti_3C_2 in T-Z-350 has not been oxidized, which is consistent with the conclusion of XRD.

Table 1 TiO_2 content of different catalysts

Samples	T-400	T-Z-350	T-Z-400	T-Z-450
TiO_2 content (wt%)	93.709	78.313	91.996	94.769

TEM analysis

Figure 2A is a TEM image of T-Z-400, and Fig. 2b is a magnified view of Fig. 2a. As shown in the figure, TiO_2 presents irregular morphology, located on the surface of carbon and embedded in the middle of carbon. Figure 2c is the local HRTEM image of Fig. 2b. TEM image shows that the lattice spacing of it is about 0.35 nm, corresponding to the (101) crystal plane of anatase TiO_2 [40]. It can be seen that Ti_3C_2 has been completely transformed into C–TiO_2. Moreover, the existence of other crystal phases, including Ti_3C_2, ZnO and Zn_2TiO_4, was not determined in multiple locations.

SEM analysis

The morphology of the photocatalysts plays an important role in the catalytic activity. The microstructures of the photocatalysts were further observed by SEM. Figure 3a shows the microscopic morphology of raw Ti_3AlC_2, showing obvious massive structure as shown in Fig. 3b, the as-prepared Ti_3C_2 had an "accordion" structure after exfoliation [41–43], and the interlayers distance can be clearly observed. The surface of Ti_3C_2 after calcination became rough, and small particles formed on it (see Fig. 3c, d). Figure 3c is the SEM image of T-400. The surface particles are larger, and "accordion" structure disappears. Figure 3d shows the SEM image of T-Z-400 prepared by molten salt method. Comparing

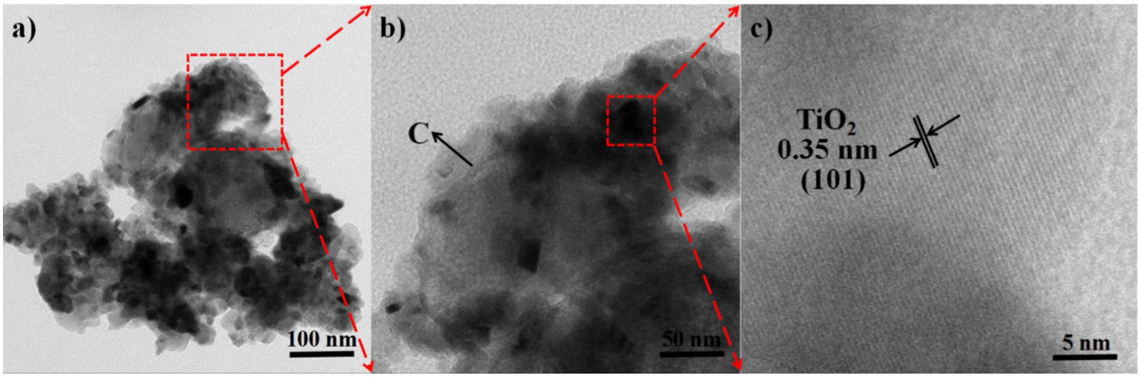

Figure 2 TEM image of b T-Z-400, **b** Partial enlargement, **c** Partial enlargement.

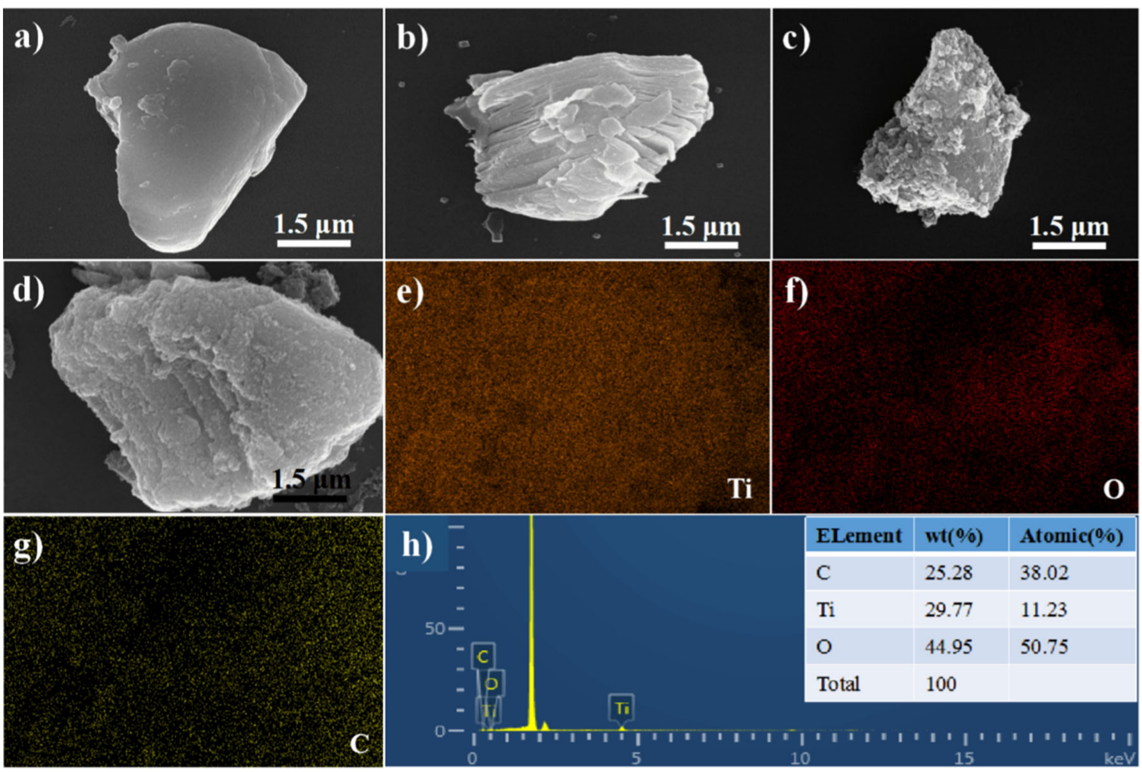

Figure 3 SEM image of **a** Ti_3AlC_2, **b** Ti_3C_2, **c** T-400, **d** T-Z-400, **e** Ti element, **f** O element, **g** C element, **h** EDX spectra of T-Z-400.

Fig. 3c, d, it can be seen that the addition of $ZnCl_2$ helps to maintain the "accordion" structure, and the TiO_2 nanoparticles with the same particle size are uniformly attached to the surface and between the layers of the disordered graphite sheets. According to EDS analysis (see Fig. 3e–g), T-Z-400 samples contained three elements: Ti, C and O, further confirming that the samples are C–TiO_2. Figure 3h is the EDS spectrum of T-Z-400 sample. No other elements are introduced into the sample by molten salt method except for O element, and XPS also confirms this (Fig. 4).

XPS analysis

The elemental states of T-Z-400 and T-400 samples were characterized by XPS. Ti2p curves in Fig. 4a were fitted into two peaks: 458.33 eV (Ti $2p_{3/2}$) and 464.03 eV (Ti $2P_{1/2}$) attributing to Ti–O bond of TiO_2 [44]. As can be seen from Fig. 4b, C1s spectrum shows two obvious peaks at 284.4 eV and 287.78 eV, which are the characteristic peaks of C–C bond and C–O bond, respectively. The relative strength of C–C bond is relatively high, indicating that C–C bond is the main form of C in the sample. The C–O bond

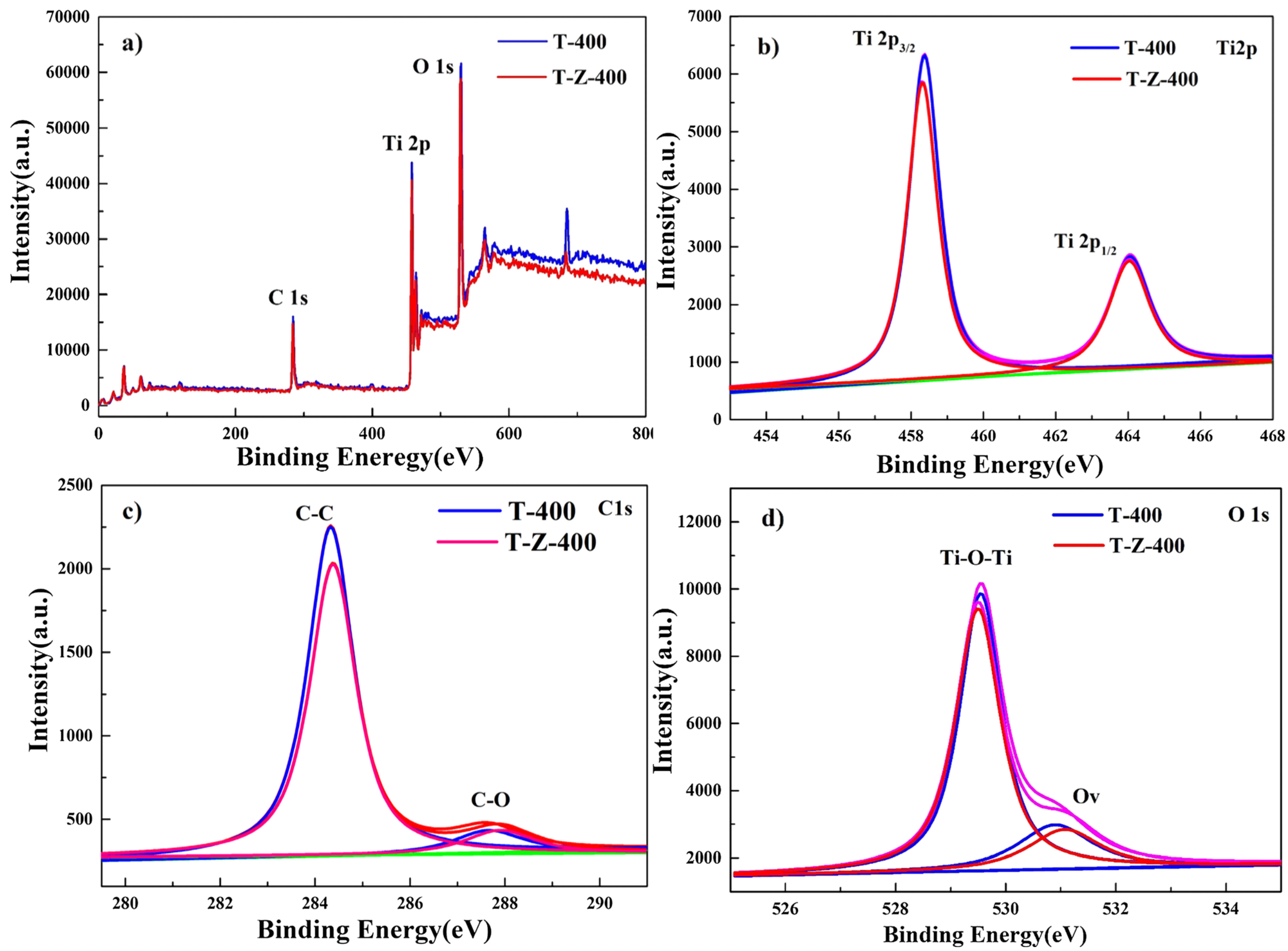

Figure 4 .High-resolution XPS spectra of T-Z-400 and T-400 **a** survey spectrum; **b** Ti 2p; **c** C 1 s; **d** O 1 s.

exists but no C=O or C–O–T band detected indicates that there is no carbon doping in T-Z-400 sample [45–47]. As is shown in Fig. 4c, regarding O1s XPS spectrum, the peak at 529.58 eV is attributed to Ti–O–Ti (lattice oxygen), and the small peak at 531.1 eV indicates the existence of partial oxygen vacancies in T-Z-400 sample. Figure 4d–f shows the Ti2p, C1s and O1s curves of T-400 sample. By comparison with the XPS diagram of T-Z-400 prepared by molten salt method and T-400, almost no difference in element distribution and bonding is detected.

Moreover, the characteristic peaks of the T-Z-400 sample are in full agreement with those of anatase TiO_2 in the XRD pattern and each diffraction peak does not shift, which indicates that no other crystalline substances exists in the sample and the element doping can be excluded. SEM mapping results show that there three elements of Ti, C and O exist, while Zn element is absent. According to the XPS characterization analysis in previous literature, Zn 2p owns corresponding peaks at 1028 and 1052 eV, however, which were not detected in of T-Z-400 sample (see full spectrum Fig. S2).

FT-IR analysis

Figure 5 shows the FT-IR diagram of the obtained samples, whose locations absorption peaks are nearly the same (wave number 1171 cm^{-1}). It may be caused by the stretching vibration of C–C bond indicating that all the samples contain carbon layer.

Raman analysis

The structural information of C–TiO_2 and the carbon existence were further identified by Raman scattering measurement. In Fig. 6, seven vibration spectra appear for the T-Z-400 and T-400 samples. The characteristic peaks of 150 cm^{-1}, 202 cm^{-1}, 391 cm^{-1},

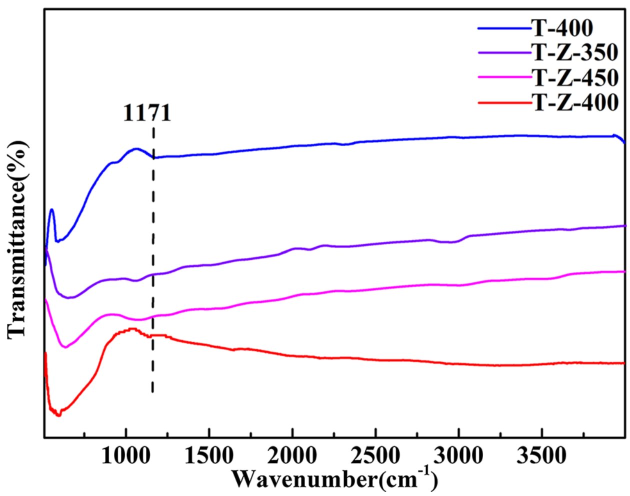

Figure 5 The FT-IR spectra of T-Z-350, T-Z-400, T-Z-450 and T-400.

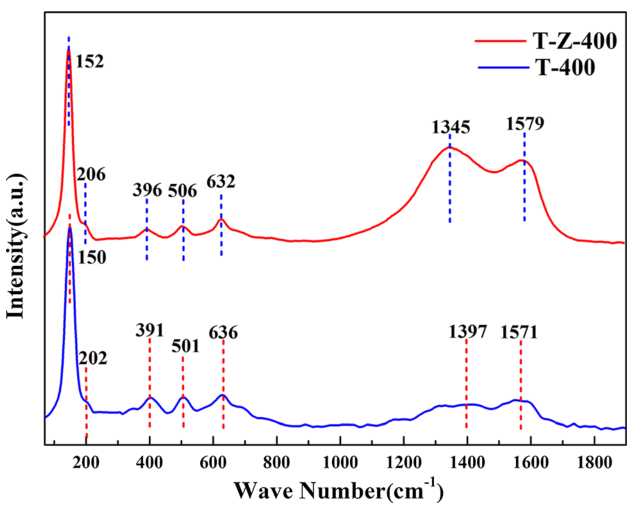

Figure 6 Raman pattern of T-Z-400 and T-400.

501 cm^{-1} and 636 cm^{-1} belong to anatase type TiO_2, which was consistent with the XRD results. There were two characteristic peaks of graphite carbon at 1571 cm^{-1} (G band) and disordered graphite structure 1397 cm^{-1} (the D band), respectively, which indicates the existence of free carbon phase. A slight difference in the intensity of two bands (I_D and I_G) of the T-Z-400 and T-400 is observed. Composite catalyst prepared without molten salts is able to promote graphitization, but the carbon production is relatively higher for the composite catalyst by molten salt method. Based on the XRD, XRF, TEM, and XPS results above, it can be confirmed that Ti_3C_2 almost chemically converted to TiO_2 and C at calcination temperatures higher than 400 °C using the molten salt method.

UV–Vis analysis

DRS and the calculated band gap are presented in Fig. 7. Analysis of Fig. 7a shows that all Ti_3C_2 MXene-derived C–TiO_2 samples exhibited significantly enhanced absorbance in the ultraviolet region. The Ti_3C_2 shows absorption of the visible region, due to its black color [48]. The absorption capacity of T-Z-400 in visible light region is the highest, which may be due to the low crystallinity of TiO_2 nanoparticles after the addition of $ZnCl_2$. Although some C has been doped into TiO_2 according to the XPS results, C–TiO_2 (T-Z-400 with the determined band gap width 3.05 eV) has obvious absorption to UV light but almost no absorption to visible light, as shown in Fig. 7b. The influence of doping on energy band greatly depends on doping position and amount [49, 50], which needs further investigations.

PL analysis

In order to further understand the photocatalytic mechanism of C–TiO_2 photocatalyst, the photoelectron–hole pair recombination behavior was investigated by photoluminescence (PL). The corresponding results are shown in Fig. 8. The spectra of all samples were tested at 350 nm excitation wavelength. It was well known that the weaker emission peak reflects the better separation of photogenerated charge, which indicates a more efficient photocatalytic performance [51]. The intensity of T-Z-400 emission peak was lower than that of T-400, which proves that T-Z-400 has better separation efficiency of photogenerated carriers.

Electrochemical analysis

In Fig. 9a, the transient photocurrent response of all samples is shown. The T-Z-400 exhibits the highest photocurrent response (photocurrent density 0.67 μA/cm^2), indicating a good interfacial charge transfer [52]. And the charge transfer resistance of the samples was determined through Nyquist plots of electrochemical impedance spectroscopy (Fig. 9b). The T-Z-400 has the smallest arc radius, which means it has the least resistance during charge transfer. Figure 9c, d is the Mott–Schottky M–S diagram of T-400

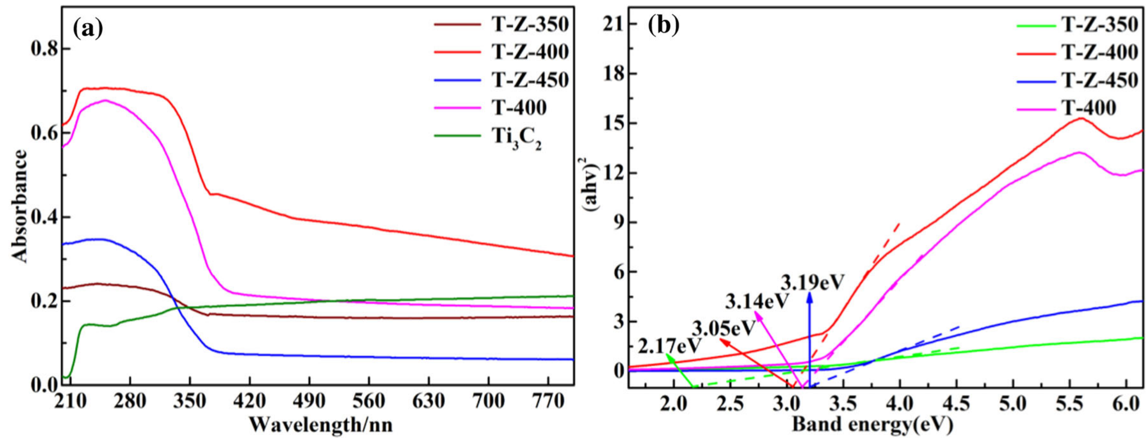

Figure 7 **a** DRS spectra of C–TiO_2 and Ti_3C_2, **b** band gap distribution of C–TiO_2.

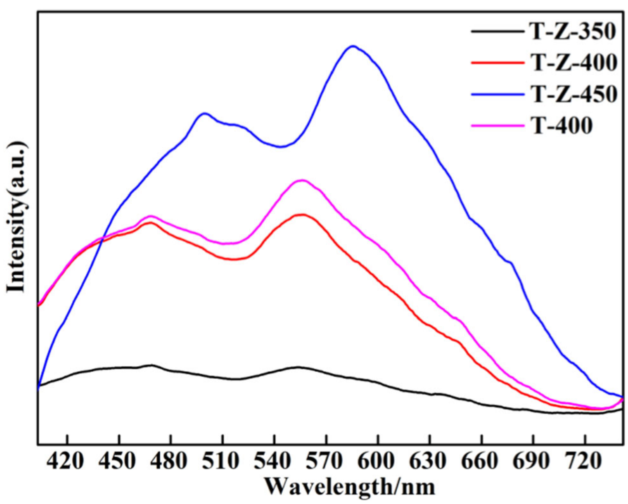

Figure 8 Photoluminescence spectra of photocatalyst.

and T-Z-400 sample, respectively, which shows that the flat band potentials of T-400 and T-Z-400 are − 0.69 eV and − 0.66 eV. Considering that the potential difference between saturated calomel electrode and standard hydrogen electrode is 0.245 eV, therefore, the conduction band potential of T-400 and T-Z-400 is calculated to be − 0.445 eV and − 0.415 eV (vs. NHE, pH = 7), respectively, which is more negative than the reduction potentials of hydrogen and meets the thermodynamic requirements of photocatalytic hydrogen production. Combined with the band gap widths, we can conclude that the valence band potential of T-400 and T-Z-400 samples is 2.695 eV and 2.635 eV respectively (vs. NHE, pH = 7). Figure 9 reveals that T-Z-400 has higher photogenerated carrier separation efficiency and faster charge transfer efficiency [53].

The series resistance (*Rs*), parallel resistance (*Rct*) and capacitance (CPE) of the sample were obtained by simulation software fitting based on the equivalent circuit diagram in EIS diagram. As shown in Table 2, T-Z-400 sample has the minimum resistance and maximum capacitance, which proves that T-Z-400 has the highest electrochemical activity.

BET analysis

N_2 adsorption–desorption isotherms and pore size distribution of Ti_3C_2, T-400 and T-Z-400 are shown in Fig. 10. A distinct hysteresis loop between adsorption and desorption could be observed in Fig. 10a, which demonstrates the presence of a mesopore (2–50 nm). It is observed in Fig. 10b that the pore size distributions of Ti_3C_2, T-400 and T-Z-400 are very similar. The high specific surface area and mesoporous structure of T-Z-400 samples enable it to have more light adsorption and active sites, which is conducive to improving the photocatalytic activity [54].

Table 3 shows that the specific surface area and pore volume of T-400 and T-Z-400 are significantly increased compared with Ti_3C_2, which is attributed to the formation of a large number of nanosized TiO_2 particles after calcination (confirmed by XRD and XRF) and leaving structural defects by oxidation. Compared with T-400, the increase in pore volume and pore size of T-Z-400 may be caused by the increased interlayer space due to the addition of $ZnCl_2$. And the proportion of pores with larger size in T-Z-400 is relatively large as shown in Fig. 10b). It is worth noting that the SBET of T-400 is higher than that of T-Z-400, which may be affected by the

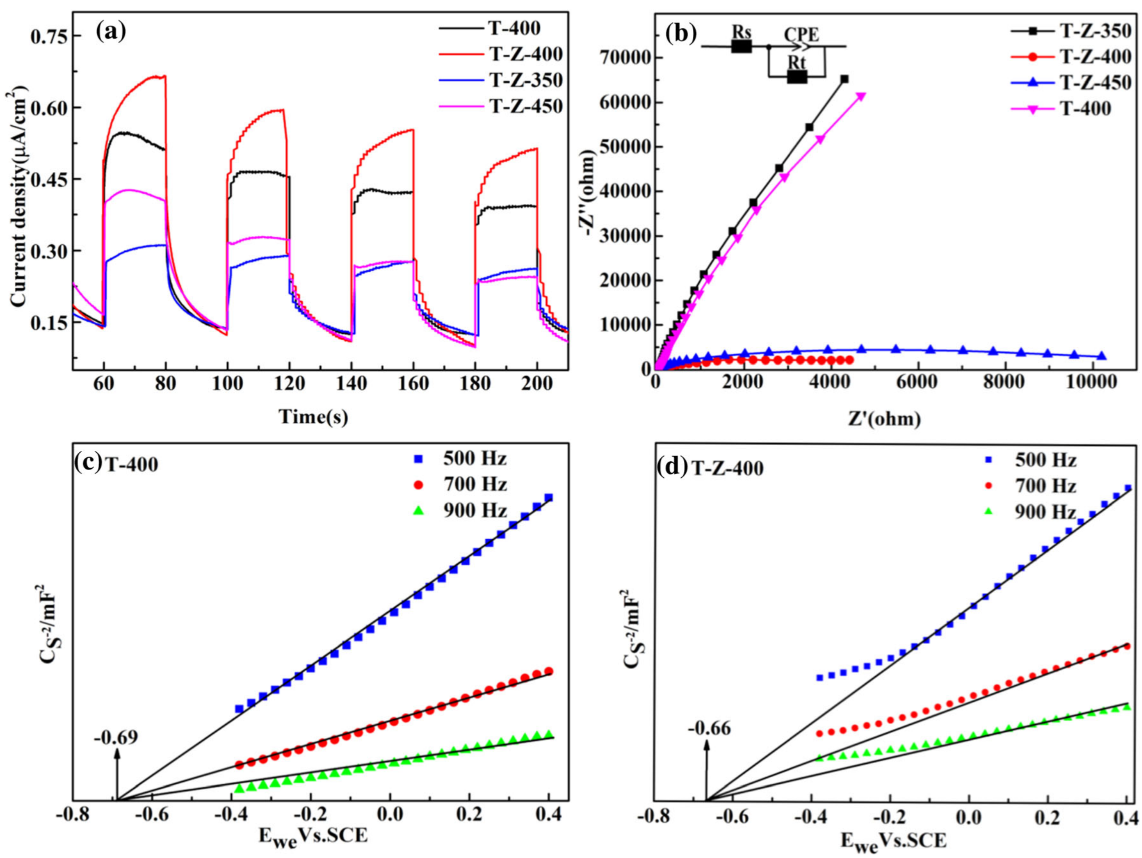

Figure 9 **a** Photocurrent response profiles, **b** electrochemical impedance spectrum, **c** Mott–Schottky plot of T-400, **d** Mott–Schottky plot of T-Z-400.

Table 2 The fitting data of EIS

	T-Z-350	T-Z-400	T-Z-450	T-400
Rs (Ω)	25.74	18.78	25.49	20.3
Rct (Ω)	6.499E+5	45.15	9466	5.283E+5
CPE (μF/cm^2)	2.189E−5	4.613E−5	3.108E−5	2.13E−5

difference in the generated TiO_2 (including content, crystallinity, size and intercrystalline pore). And the amount of residual carbon and its structural defects also affected the SBET. On the whole, the deep oxidation of Ti_3C_2 increased the overall specific surface area of the catalyst, and the supplemental XRF characterization (Table 1) showed that the TiO_2 content of T-400 was much greater than that of T-Z-400, thus resulting in a higher SBET. The high activity of T-Z-400 at a lower specific surface area indicates that composition and structure of the composite catalyst play a more dominant role in the activity.

Photocatalytic activity

The photocatalytic activity of C–TiO_2 was evaluated under full spectral irradiation. Figure 11a shows the comparison of photocatalytic H_2 production activities of T-Z-350, T-Z-400, T-Z-450 and T-400. With the increase of calcination temperature, H_2 production efficiency increases first and then decreases. This may be because the low calcination temperature of T-Z-350 results in less TiO_2 content and low absorbance. The higher calcination temperature of T-Z-450 increases the crystallinity of TiO_2, but excessive TiO_2 stacked together without intimate combination with disordered graphite sheets will affect the mobility of photogenerated electrons, thus limiting the utilization of light. T-Z-400 has the highest H_2 production efficiency of 2.3 mmol/h/g, 5.4 times that of T-400 and twice that of P25. As shown in Fig. 11b, T-400 exhibits H_2 evolution rate as low as 0.425 mmol/h/g, which may be due to the collapse of disordered graphite sheets in the calcination process, resulting in the decrease of pore volume and aperture, thus to

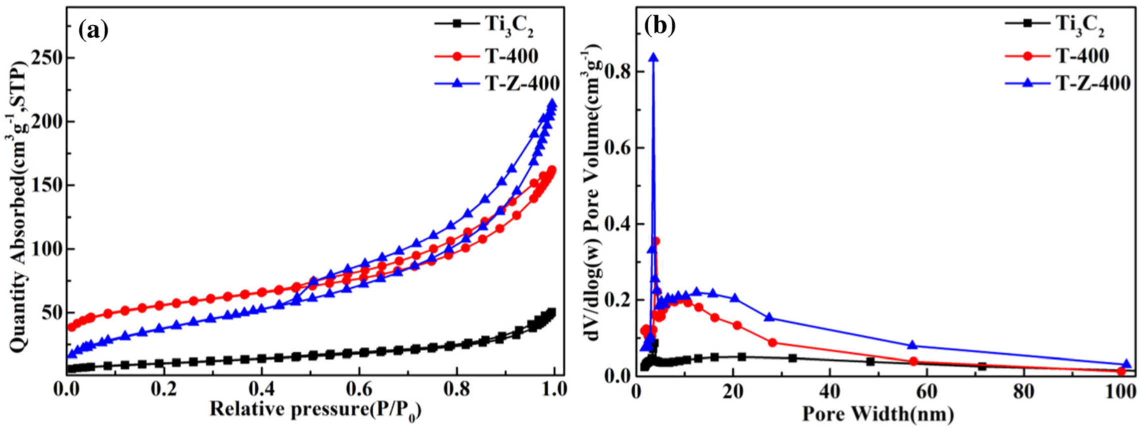

Figure 10 **a** N_2 adsorption–desorption isotherms of Ti_3C_2, T-400 and T-Z-400, **b** pore size distribution of Ti_3C_2, T-400 and T-Z-400.

Table 3 Specific surface area, pore volume and pore size distribution

Sample	S_{BET} (m^2/g)	V_{total} (cm^3/g)	D (nm)
Ti_3C_2	36.74	0.074	8.07
T-400	197.82	0.24	4.92
T-Z-400	138.32	0.31	8.81

lower the migration rate of photocarriers and the activity of photocatalytic reaction. In addition, T-Z_l-400 and T-Z_m-400 exhibit 0.879 and 2.291 mmol/h/gH_2 evolution rate, respectively, which indicates that little different exists in the hydrogen production activity for the prepared catalysts calcined within the enough molten salts. However, insufficient molten salts reduced the catalytic activity of the catalysts, where the calcination environment was close to that without molten salts.

Cycling photocatalytic stability over T-Z-400 seems not meet expectations (Fig. S3). The photocatalytic H_2 production shows a significant attenuation caused by the pore-like structural damage (Fig. S4) on the sample surface even in the sample interior after 3 cyclic runs of photocatalytic H_2 production. The cause and avoidance of such performance attenuation and structural damage may be the focus of the subsequent research.

Photocatalytic mechanism

Figure 12 is a schematic diagram of the photocatalytic hydrogen generation mechanism of C–TiO_2. The carbon produced plays an important role. On the one hand, under sunlight irradiation, according to the basic principle of photocatalytic semiconductor, electrons from the valence band of TiO_2 transfer to the conduction band. Due to the good electrical conductivity of amorphous carbon, electrons will be

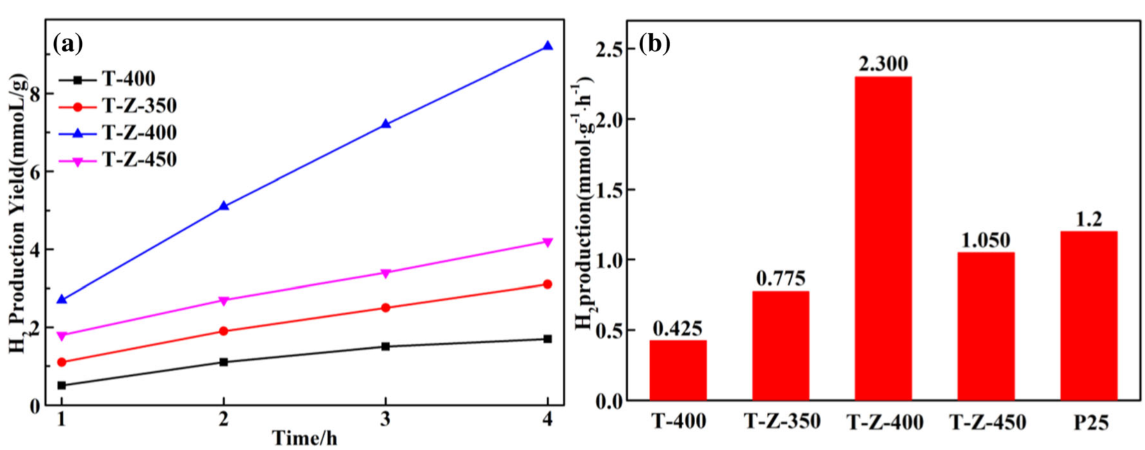

Figure 11 **a** Photocatalytic H_2 production for C–TiO_2, **b** H_2 production histogram.

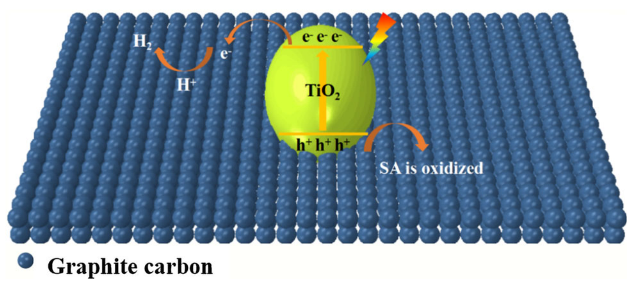

Figure 12 The schematic illustration of photocatalytic hydrogen production of C–TiO_2.

further transferred to the graphite carbon and react with H^+ and H_2O to produce H_2, while the H^+ in the valence band will be consumed by the triethanolamine reaction. The effect of the produced graphite carbon is better than Ti_3C_2, which can be confirmed by our experimental results and others [33]. On the other hand, the formation of carbon can change the overall light absorption of the catalyst. XPS results confirm that under our experimental conditions, part of C–O bonds formed, and C replaced Ti, which did not promote the absorption of visible light. Therefore, experimental conditions may be further optimized in the future to solve the problem of visible light absorption. Moreover, more reaction sites can be added only when TiO_2 grows uniformly on amorphous graphite carbon instead of stacking. The addition of $ZnCl_2$ has a certain effect on the expansion of layer spacing, and molten salt can inhibit the abnormal growth of TiO_2 grain, thus reducing the grain size. In summary, the recombination efficiency of photoelectron–hole pair is reduced and the process of photocatalytic hydrogen production is accelerated.

Conclusions

In conclusion, we successfully prepared C–TiO_2 composite photocatalyst by using Ti_3C_2 as precursor through simple molten salt method. The TiO_2 is located between disordered graphite sheets, which facilitates the separation of photogenerated carriers. The calcination temperature has a certain effect on the optical and photocatalytic properties. T-Z-400 exhibits significant hydrogen evolution activity due to suitable light absorption, low photocarrier recombination rate, high electron transfer efficiency, and abundant active sites. Using 3 wt% Pt as cocatalyst, T-Z-400 showed excellent photocatalytic hydrogen production performance of 2.3 mmol/g/h. This study opens up a new idea for the preparation of high efficiency and low-cost TiO_2 base photocatalysts with Ti_3C_2. It is believed that the most important role of $ZnCl_2$ is to delay the oxidation rate; therefore, it ensures that when Ti_3C_2 is completely oxidized to TiO_2, the TiO_2 has relatively smaller grains and more C retains, which led to a suitable composition of the catalyst, so as to obtain a better hydrogen production performance.

Acknowledgements

This work is financially supported by the National Natural Science Foundation of China (No. 22178077) and Heilongjiang Provincial Natural Science Foundation of China (No. LH2020B013).

Declarations

Conflict of interest The authors declare that they have no conflict of interest.

Supplementary Information: The online version contains supplementary material available at https://doi.org/10.1007/s10853-022-07991-2.

References

[1] Uribe-Toril J, Ruiz-Real JL, Milán-García J, de Pablo Valenciano J (2019) Energy, economy and environment: a worldwide research update. Energies 12(6):1120

[2] Wang ZP, Lin ZP, Shen SJ, Zhong WW, Cao SW (2021) Advances in designing heterojunction photocatalytic materials. Chinese J Catal 42(5):710–730

[3] Chong MN, Jin B, Chow CWK, Saint C (2010) Recent developments in photocatalytic water treatment technology: a review. Water Res 44(10):2997–3027

[4] Fujishima A, Honda K (1972) Electrochemical photolysis of water at a semiconductor electrode. Nature 238(5358):37–38

[5] Song H, Li CX, Lou ZR, Ye ZZ, Zhu LP (2017) Effective formation of oxygen vacancies in black TiO_2 nanostructures with efficient solar-driven water splitting. ACS Sustain Chem Eng 5(10):8982–8987

[6] Huang KL, Li CH, Li HZ, Ren GM, Wang L, Wang WT, Meng XC (2020) Photocatalytic applications of two-dimensional Ti_3C_2 MXenes: a review. ACS Appl Nano Mater 3(10):9581–9603

[7] Wang XJ, Zhang GZ, Yang L, Sharman E, Jiang J (2018) Material descriptors for photocatalyst/catalyst design. Wires Comput Mol Sci 8(5):e1369

[8] Zhao YX, Zhang S, Shi R, Waterhouse GIN, Tang JW, Zhang TR (2020) Two-dimensional photocatalyst design: a critical review of recent experimental and computational advances. Mater Today 34:78–91

[9] Chen X, Mao SS (2007) Titanium dioxide nanomaterials: synthesis, properties, modifications, and applications. Chem Rev 107(7):2891–2959

[10] Low JX, Qiu SQ, Xu DF, Jiang CJ, Cheng B (2018) Direct evidence and enhancement of surface plasmon resonance effect on Ag-loaded TiO_2 nanotube arrays for photocatalytic CO_2 reduction. Appl Surf Sci 434:423–432

[11] Pham TD, Lee BK (2017) Novel photocatalytic activity of Cu@V co-doped TiO_2/PU for CO_2 reduction with H_2O vapor to produce solar fuels under visible light. J Catal 345:87–95

[12] Chung KH, Jeong SM, Kim BJ, An KH, Park YK, Jung SC (2018) Enhancement of photocatalytic hydrogen production by liquid phase plasma irradiation on metal-loaded TiO_2/-carbon nanofiber photocatalysts. Int J Hydrogen Energy 43(24):11422–11429

[13] Zhang X, Chen YJ, Xiao YT, Zhou W, Tian GH, Fu HG (2018) Enhanced charge transfer and separation of hierarchical hydrogenated TiO_2 nanothorns/carbon nanofibers composites decorated by NiS quantum dots for remarkable photocatalytic H_2 production activity. Nanoscale 10:4041–4050

[14] Yan X, Xing ZP, Cao Y, Hu MQ, Li ZZ, Wu XY, Qi Z, Yang SL et al (2017) In-situ C-N-S-tridoped single crystal black TiO_2 nanosheets with exposed 001 facets as efficient visible-light-driven photocatalysts. Appl Catal B-Environ 219:572–579

[15] Khazaei M, Arai M, Sasaki T, Chung C-Y, Venkataramanan NS, Estili M, Sakka Y, Kawazoe Y (2013) Novel electronic and magnetic properties of two-dimensional transition metal carbides and nitrides. Adv Funct Mater 23(17):2185–2192

[16] Gao YP, Wang LB, Zhou AG, Li ZY, Chen JK, Bala H, Hu QK, Cao XX (2015) Hydrothermal synthesis of TiO_2/Ti_3C_2 nanocomposites with enhanced photocatalytic activity. Mater Lett 150:62–64

[17] Anasori B, Luhatskaya MR, Gogotsi Y (2017) 2D metal carbides and nitrides (MXenes) for energy storage. Nat Rev Mater 2(10):16098

[18] Naguib M, Kurtoglu M, Presser V, Lu J, Niu JJ, Heon M, Hultman L, Gogotsi Y et al (2011) Cheminform abstract: two-dimensional nanocrystals produced by exfoliation of Ti_3AlC_2. Adv Mater 23:4248–4253

[19] Ke T, Shen SY, Rajavel K, Yang K, Lin DH (2021) In situ growth of TiO_2 nanoparticles on nitrogen-doped Ti_3C_2 with isopropyl amine toward enhanced photocatalytic activity. J Hazard Mater 402:124066

[20] Peng C, Zhou T, Wei P, Ai H, Zhou B, Pan H, Xu WK, Jia JB, Zhang K, Wang HJ, Yu H (2022) Regulation of the rutile/anatase TiO_2 phase junction in-situ grown on –OH terminated $Ti_3C_2T_x$ (MXene) towards remarkably enhanced photocatalytic hydrogen evolution. Chem Eng J 439:135685

[21] Xie X, Zhang N (2020) Positioning MXenes in the photocatalysis landscape: competitiveness, challenges, and future perspectives. Adv Funct Mater 30(36):2002528

[22] Peng C, Yang X, Li Y, Yu H, Wang H, Peng F (2016) Hybrids of two-dimensional Ti_3C_2 and TiO_2 exposing {001} facets toward enhanced photocatalytic activity. ACS Appl Mater Interfaces 8(9):6051–6060

[23] Wang H, Peng R, Hood ZD, Naguib M, Adhikari SP, Wu Z (2016) Titania composites with 2D transition metal carbides as photocatalysts for hydrogen production under visible-light irradiation. Chemsuschem 9(12):1490–1497

[24] Peng C, Wei P, Li X, Liu Y, Cao Y, Wang H, Yu H, Peng F, Zhang LY, Zhang BS, Lv K (2018) High efficiency photocatalytic hydrogen production over ternary Cu/TiO_2@$Ti_3C_2T_x$ enabled by low-work-function 2D titanium carbide. Nano Energy 53:97–107

[25] Low J, Zhang L, Tong T, Shen B, Yu J (2018) TiO_2/MXene Ti_3C_2 composite with excellent photocatalytic CO_2 reduction activity. J Catal 361:255–266

[26] Peng C, Zhou T, Wei P, Yan X, Kong Y, Xu W, Wang HJ, Yu H, Jia JB, Zhang K, Pan H (2022) Steering interfacial charge kinetics: synergizing cocatalyst roles of $Ti_3C_2M_x$ (MXene) and NCDs for superior photocatalytic performance over TiO_2. Appl Surf Sci 599:154001

[27] Peng C, Xie X, Xu W, Zhou T, Wei P, Jia JB, Zhang K, Cao YH, Wang HJ, Peng F, Yang R, Yan XQ, Pan H, Yu H (2021) Engineering highly active Ag/Nb_2O_5@Nb_2CT_x (MXene) photocatalysts via steering charge kinetics strategy. Chem Eng J 421:128766

[28] Peng C, Zhou T, Wei P, Xu WK, Pan H, Peng F, Jia JB, Zhang K, Yu H (2021) Photocatalysis over MXene-based hybrids: synthesis, surface chemistry, and interfacial charge kinetics. Apl Mater 9(7):070703

[29] Xu WK, Li XY, Peng C, Yang GX, Cao YH, Wang HJ, Peng F, Yu H (2022) One-pot synthesis of Ru/Nb_2O_5@Nb_2C ternary photocatalysts for water splitting by harnessing hydrothermal redox reactions. Appl Catal B Environ 303:120910

[30] Yin JJ, Zhan FK, Jiao TF, Wang WH, Zhang GC, Jiao JH, Jiang GY, Zhang QR et al (2020) Facile preparation of self-assembled MXene@Au@CdS nanocomposite with

enhanced photocatalytic hydrogen production activity. Sci China Mater 63(11):2228–2238

[31] Jia GR, Wang Y, Cui XQ, Zheng WT (2018) Highly carbon-doped TiO_2 derived from MXene boosting the photocatalytic hydrogen evolution. ACS Sustain Chem Eng 6(10):13480–13486

[32] Yuan WY, Cheng LF, Zhang YN, Wu H, Lv SL, Chai LY, Guo XH, Zheng LX (2017) Hydrogen evolution: 2D-Layered carbon/TiO_2 hybrids derived from Ti_3C_2 MXenes for photocatalytic hydrogen evolution under visible light irradiation. Adv Mater Interfaces 4(20):1700577

[33] Naguib M, Mashtalir O, Lukatskaya MR, Dyatkin B, Zhang CF, Presser V, Gogotsi Y, Barsoum MW et al (2014) One-step synthesis of nanocrystalline transition metal oxides on thin sheets of disordered graphitic carbon by oxidation of MXenes. Chem Commun 50(56):7420–7423

[34] Ding XH, Li YC, Li CH, Wang WT, Wang L, Feng LJ, Han DZ (2019) 2D visible-light-driven TiO_2@Ti_3C_2/g-C_3N_4 ternary heterostructure for high photocatalytic activity. J Mater Sci 54:9385–9396. https://doi.org/10.1007/s10853-018-03289-4

[35] Wang S, Zhao L, Bai LN, Yan JM, Jiang Q, Lian JS (2014) Enhancing photocatalytic activity of disorder-engineered C/TiO_2 and TiO_2 nanoparticles. J Mater Chem A 2(20):7439–7445

[36] Yang CW, Zhang XY, Qin JQ, Shen X, Yu RC, Ma MZ, Liu RP (2017) Porous carbon-doped TiO_2 on TiC nanostructures for enhanced photocatalytic hydrogen production under visible light. J Catal 347:36–44

[37] Yoon KH, Cho YS, Kang DH (1998) Review molten salt Synthesis of lead-based relaxors. Mater Sci 33(12):2977–2984

[38] Ma TY, Cao JL, Jaroniec M, Qiao SZ (2016) Interacting carbon nitride and titanium carbide nanosheets for high-performance oxygen evolution. Angew Chem Int Ed 128(3):1150–1154

[39] Ušáková M, Lukáč J, Dosoudil R, Jančárik V, Grusková A, Ušák E, Sláma J, Šubrt J (2007) Influence of Cu^{2+} ions on structural and magnetic properties of NiZn ferrites. J Mater Sci Mater Electron 18(12):1183–1189

[40] Hu XL, Lu SC, Tian J, Wei N, Song XJ, Wang XZ, Cui HZ (2018) The selective deposition of MoS_2 nanosheets onto (101) facets of TiO_2 nanosheets with exposed (001) facets and their enhanced photocatalytic H_2 production. Appl Catal B Environ 241:329–337

[41] Li YJ, Yin ZH, Ji GR, Liang ZQ, Xue YJ, Guo YC, Tian J, Wang XZ et al (2019) 2D/2D/2D heterojunction of Ti_3C_2 MXene/MoS_2 nanosheets/TiO_2 nanosheets with exposed (001) facets toward enhanced photocatalytic hydrogen production activity. Appl Catal B Environ 246:12–20

[42] Alhabeb M, Maleski K, Anasori B, Lelyukh P, Clark L, Sin S, Gogotsi Y (2017) Guidelines for synthesis and processing of two-dimensional titanium carbide ($Ti_3C_2T_x$ MXene). Chem Mater 29(18):7633–7644

[43] Peng J, Chen XZ, Ong WJ, Zhao XJ, Li N (2019) Surface and heterointerface engineering of 2D MXenes and their nanocomposites: insights into electro- and photocatalysis. Chem 5(1):18–50

[44] Lukowski MA, Daniel AS, Fei M, Meng F, Forticaux A, Li L, Jin S (2013) Enhanced hydrogen evolution catalysis from chemically exfoliated metallic MoS_2 nanosheets. J Am Chem Soc 135(28):10274–10277

[45] Zhao L, Chen XF, Wang XC, Zhang YJ, Wei W, Sun YH, Antonietti M, Titirici MM (2010) One-step solvothermal synthesis of a carbon@TiO_2 dyade structure effectively promoting visible-light photocatalysis. Adv Mater 22(30):3317–3321

[46] Ren WJ, Ai ZH, Jia FL, Zhang LZ, Fan XX, Zou ZG (2007) Low temperature preparation and visible light photocatalytic activity of mesoporous carbon-doped crystalline TiO_2. Appl Catal B Environ 69:138–144

[47] Park Y, Kim W, Park H, Tachikawa T, Majima T, Choi W (2009) Carbon-doped TiO_2 photocatalyst synthesized without using an external carbon precursor and the visible light activity. Appl Catal B Environ 91(1):355–361

[48] Ran JR, Gao GP, Li FT, Ma TY, Du A, Qiao SZ (2017) Ti_3C_2 MXene co-catalyst on metal sulfide photo-absorbers for enhanced visible-light photocatalytic hydrogen production. Nat Commun 8:13907

[49] Yang HR, Tian J, Bo YY, Zhou YL, Wang XZ, Cui HZ (2017) Visible photocatalytic and photoelectrochemical activities of TiO_2 nanobelts modified by In_2O_3 nanoparticles. Colloid Interface 487:258–265

[50] Wang YB, Zhang YN, Zhao GH, Tian HY, Shi HJ, Zhou TC (2012) Design of a novel CuO/TiO/carbon aerogel electrode and its efficient electrosorption-assisted visible light photocatalytic degradation of 2,4,6-trichlorophenol. ACS Appl Mater Interfaces 4(8):3965–3972

[51] Yang CW, Qin JQ, Xue Z, Ma MZ, Zhang XY, Liu RP (2017) Rational design of carbon-doped TiO_2 modified g-C_3N_4 via in-situ heat treatment for drastically improved photocatalytic hydrogen with excellent photostability. Nano Energy 41:1–9

[52] Xiao TT, Tang Z, Yang Y, Tang L, Zhou Y, Zou ZG (2018) In situ construction of hierarchical WO_3/g-C_3N_4 composite hollow microspheres as a Z-scheme photocatalyst for the degradation of antibiotics. Appl Catal B Environ 220:417–428

[53] Cui DD, Wang L, Xu K, Ren L, Wang L, Yu YX, Du Y, Hao WC (2018) Band-gap engineering of BiOCl with oxygen

vacancies for efficient photooxidation properties under visible-light irradiation. J Mater Chem A 6:2193–2199

[54] Cui YJ, Zhang GG, Lin ZZ, Wang XC (2016) Condensed and low-defected graphitic carbon nitride with enhanced photocatalytic hydrogen evolution under visible light irradiation. Appl Catal B Environ 181:413–419